Atmospheric Environment 327 (2024) 120495

Contents lists available at ScienceDirect

Atmospheric Environment

journal homepage: www.elsevier.com/locate/atmosenv

An improved approach to determine aerosol properties from all-sky camera imagery: Sensitivity to the partially cloud scenes

F. Scarlatti [a,*], J.L. Gómez-Amo [a], P.C. Valdelomar [a], V. Estellés [a,b], M.P. Utrillas [a]

[a] Departament de Física de la Terra i Termodinámica, Universitat de València, Carrer Doctor Moliner, 50, Burjassot, 46100, Spain
[b] ISAC-CNR, Via Fosso del Cavaliere 100, Rome, 00133, Italy

HIGHLIGHTS

- Retrieval of aerosol properties AOD and AE in presence of partially cloudy sky.
- Calibrated all-sky camera RGB signals related to Cimel direct aerosol properties with machine learning methodology.
- Statistical evaluation of prediction performances of machine learning method.
- Aerosol retrieval in partially cloud retrieval can help indirect effect studies.

ARTICLE INFO

Keywords:
Aerosol properties
Partially cloud scenarios
All-sky camera
AOD and AE
Machine Learning

ABSTRACT

We present a new approach to determine aerosol properties from radiometrically calibrated images provided by an all-sky camera. It is designed to be used regardless of the sky conditions. However, we especially focus on partially cloudy scenes, which is the main novelty of this work. Our methodology is based on using a small sector of the image that contains the principal plane of the Sun. The RGB principal plane radiances are associated to the aerosol optical depth (AOD) and Angstrom exponent (AE) AERONET observations through a Gaussian Process Regression (GPR) machine learning (ML) model. We identify the cloudy points within our working sector and the principal plane signal for the RGB radiances is averaged and smoothed. Then, we use the Pérez model to synthesize the principal plane signal in the cloudy spots. Finally, 2-year dataset has been used to test the method considering different atmospheric conditions related to the presence of clouds and aerosols, according to their amount and type. In addition, we have developed a method to evaluate the quality of predictions based on the standard deviation of the GPR. This quality assurance method may be fine-tuned according to the desired accuracy based on the application for which it is intended. Our AOD and AE predictions show an excellent overall agreement with AERONET measurements that substantially improves when our quality assurance method is applied. In that case, we obtain a high degree of correlation ($R^2 > 0.97$) and an overall MAE lower than the nominal uncertainty of AERONET measurements (0.006 and 0.05 for AOD and AE, respectively). Moreover, more than 83% and 77% of the predictions fall within the nominal uncertainty associated with AERONET measurements for AOD and AE, respectively. A comprehensive sensitivity analysis of the factors affecting the performance of the proposed methodology confirms that our method is stable and not very sensitive to external and methodological factors, especially when we apply quality assurance criteria. All this supports that our methodology is a reliable alternative to retrieve the optical properties of aerosols independently of the cloud conditions. Our results may contribute to the operational use of all-sky cameras, which may be an interesting complement regarding the study of aerosol-cloud interactions in partially cloud scenarios.

1. Introduction

Aerosol research is of fundamental importance in several fields of study, such as climate research and solar energy (Alexander et al., 2013). The effects of aerosol on climate are mostly due to their radiative impact associated to the direct (scattering and absorption of solar and thermal radiation) and indirect (aerosol-cloud-radiation

* Correspondence to: Department of Earth Physics and Thermodynamics, Solar Radiation Research Unit, Universitat de València, C/ Dr. Moliner 50, 46100 Burjassot (Valencia), Spain.
E-mail address: francesco.scarlatti@uv.es (F. Scarlatti).

https://doi.org/10.1016/j.atmosenv.2024.120495
Received 9 December 2023; Received in revised form 13 March 2024; Accepted 1 April 2024
Available online 6 April 2024

interactions) aerosol mechanisms (Kim and Ramanathan, 2008). The degree of uncertainty of these interactions, especially those related to the indirect processes, is too large to allow an exact determination of the global radiative effect: whether the net aerosol contribution is to cool or heat the Earth surface (Sicard et al., 2012, 2014; Eddy, 2012). Most of these uncertainties are due to the great spatiotemporal variability of the aerosol amount and properties and extensive and continuous monitoring is required. Consequently, multitude of instruments, networks and techniques have been developed in the latest decades (di Sarra et al., 2011, 2015; Laj et al., 2020). The remote sensing retrieval of aerosol properties is still a challenging task when the sky is contaminated by clouds (Eck et al., 2014; Luffarelli et al., 2022). In this sense, the presence of clouds implies difficulties depending on the observation strategies, both in the case of ground- or satellite-based measurements. For these reasons the properties of aerosols are usually determined only in cloud-free conditions (Cazorla et al., 2008, 2009). Particularly in ground-based remote sensing, retrievals using direct sun measurements perform correctly only if clouds do not cover the sun. Thus, significant efforts have been made to perform satisfactory cloud screening, minimizing, or avoiding the associated uncertainties (Smirnov et al., 2000; Giles et al., 2019; di Sarra et al., 2015). However, the retrievals based on radiance measurements from all-sky or a significant part of the sky are more affected by clouds (Cazorla et al., 2008, 2009), since clouds increase the uncertainty associated to the inversion algorithms or prevent the retrievals. Therefore, it is necessary to establish observation strategies that overcome these drawbacks. In this sense, all-sky cameras seem to be an interesting alternative for obtaining the optical properties of aerosols, both in clear sky conditions and in partially cloudy skies. All-sky cameras have a lower spectral range and resolution than sun-photometers, since they generally use only 3 broadband channels in the visible (RGB with around 100 nm bandwidth). But on the other hand, they have the advantage of measuring simultaneously the whole sky radiance with high temporal resolution (usually less than one minute). All-sky imagers were originally devoted to cloud monitoring even in dynamic scenarios, to determine cloud cover and type (González et al., 2023; Calbó et al., 2017). However, in recent years much progress has been made in its application for atmospheric research, particularly for the study of aerosols, clouds, and radiation. Thus, alternatives have been established to carry out accurate geometric and radiometric calibrations of all-sky cameras and determine their radiative uncertainty (Román et al., 2022, 2012; Valdelomar et al., 2021; Fiorentin et al., 2020). Furthermore, all-sky camera measurements have been used to determine the optical properties of aerosols and clouds in combination with radiative transfer models (Román et al., 2022; Dubovik and King, 2000; Dubovik et al., 2000; Peris-Ferrús et al., 2021a,b). The results reported by these approaches are in very good agreement with the most accurate retrievals derived from networks, such AERONET. In general, these comparisons show correlation coefficients higher than 90% and very low bias (< 10%). Another way to obtain the properties of the atmosphere involves machine learning (ML) or deep learning techniques, which are being increasingly used in atmospheric research (Yang et al., 2022; Bao et al., 2023; Tian et al., 2022; Guo et al., 2023). These techniques have been recently applied to the all-sky camera images. In general, supervised algorithms are used during the training, looking for relationship between all-sky camera images and the aerosol measurements provided from colocated sun photometers (Cazorla et al., 2008, 2009; Scarlatti et al., 2023, 2021; Logothetis et al., 2023; Mejia et al., 2015). The results obtained using these approaches concur also well with those reported by AERONET, showing the high potential of these new statistical tools in aerosol research. Our previous work is in line with this, since it combines ML techniques and images from an all-sky camera to derive the optical properties of aerosols (AOD and AE) (Scarlatti et al., 2023, 2021). In these works, only a small sector of the image was used in the retrieval, and therefore the rest of the sky could allow the presence of cloud coverage and does not affect the results. However, a very important fraction of the images (around 30%) were left out of the retrieval thanks to the strict conditions imposed to avoid the presence of clouds within the working sector of the image. For this reason, the main objective of this work is to increase the number of useful images for retrieval of aerosol properties. With this in mind, we propose a generalization of our method (Scarlatti et al., 2023) to make the all-sky camera a more versatile instrument in terms of obtaining aerosol properties in different atmospheric conditions. To do this, we have changed the approach to allow clouds within the working sector (which is currently smaller) without having a noticeable influence on the quality of our retrieval. From a methodological point of view, the way we treated the clouds in our working sector of the image constitutes the most important novelty of this work, that allows to address the study of aerosols in a greater number of sky conditions. On the other hand, we have maintained some of the assumptions used in the previous work, since they performed well and constitute the core of our retrieval methodology. Therefore, we still rely in the Gaussian Process Regression ML model since it has certain advantages from the statistical point of view and uncertainty calculations. It shows high flexibility to obtain no linear patterns hidden behind the input and output data. In addition, the algorithm itself furnish the statistical uncertainties of the physical outputs. Finally, sensitivity analysis have been carried out regarding the parameters that affect the prediction performance, showing the stability of our methodology in retrieving good quality of aerosol products.

The paper is structured as follows: in Section 2, the instruments used in this study and the characterization of their data are presented; in Section 3, we detail the methodology used for image preprocessing and the ML models; in Section 4, the results and its quality analysis are reported with a comparison with other models; and finally; in Section 5, we summarize the main conclusions of this work.

2. Site description and instrumentation

We have used data from the instrumentation deployed in the Burjassot AtmoSpheric Station (BASS), which is maintained by the Solar Radiation Group of the University of Valencia (GRSV). BASS is a ground-based measurements station located in the eastern part of Spain (39.51 N, −0.42 W) within the metropolitan area of Valencia, 10 km away from the Mediterranean coast. The measurements are focused to monitor aerosols, clouds, solar and atmospheric radiation through remote sensing and in situ instruments (Estellés et al., 2007; Segura et al., 2016; Marcos et al., 2018; Gómez-Amo et al., 2017, 2019). These instruments and measurements are involved in several international observational programs and networks, such as AERONET, SKYNET, e-profile and EARLINET. In addition, BASS belongs to ACTRIS research infrastructure. In the present work we used data from an all-sky camera and a sun-photometer. The main instrument used in this work is an all-sky camera, SONA-201-D, which has been manufactured by Sieltec Canarias S.L. The SONA has a digital body color camera using a fisheye lens. All of this is encapsulated in a thermally controlled environment housing. The sensor mounts an RGB filter and an infrared blocking window, so the images have three channels with effective wavelengths of 615 ± 6 nm, 541 ± 5 nm and 480 ± 6 nm for red, green and blue, respectively (Valdelomar et al., 2021). The camera has been characterized and set to furnish geometrically and radiometrically calibrated high dynamic range (HDR) images of the sky, with 180° field of view. Therefore, we measure the radiance coming from every portion of the sky dome, with the spatial resolution defined by the camera observation geometry in terms of pixel zenith, azimuth, and solid angles (PZA, PAA, PSA respectively). The geometrical calibration is carried out by automatically tracking celestial bodies with known trajectories in the sky, and choosing the most correlated relation between the zenith angle and the distance of the pixel from the center: a linear formula. The radiometric calibration of the HDR images is performed by comparing the raw signal against the RGB convolution of the spectral radiance obtained by radiative transfer simulations. These simulations are performed in the same atmospheric conditions as the measured HDR images, in terms of aerosols, ozone and water vapor. The relative uncertainties for the radiative calibration are 7% for the blue and green channels and 10% for the red channel. For all the related details of the SONA camera and its characterization, see (Valdelomar et al., 2021). The radiance for the three channels shows a very good agreement with the AERONET sky-radiance measurements. In clear sky conditions, the comparison shows correlation coefficients higher than 0.96 and relative differences smaller than 9%, 6% and 4% for red, green, and blue channel, respectively (Valdelomar et al., 2021). With all of this, we routinely obtain HDR images, geometrically and radiometrically calibrated, with 1-minute temporal resolution since February 2020. In addition, we used colocated direct-sun measurements from the Cimel CE-318 sun-photometer, as a reference for spectral AOD and AE. Only the AOD at 675, 500 and 440 nm (the closest wavelengths to the camera RGB channels) and AE at 675–440 nm have been considered. We have used data from the version 3 of the AERONET direct-sun algorithm, which are automatically cloud screened (Giles et al., 2019). These AERONET data have been associated to the all-sky camera measurements with a time tolerance of 15 min centered around the timestamp of the images. Having a large dataset is an important need of our ML method. Therefore, we have chosen level 1.5 data to have as much available data as possible during the limited period of our study. This limitation is due to the all-sky camera imagery which is available only since February 2020. Finally, in this work, we have used a 2-year database, from 10 February 2020 to 31 March 2022.

3. Methodology

3.1. Signal preprocessing

The methodology we follow in this work is based on Scarlatti et al. (2023). The main difference is that only clear-sky situations within the working sector of the image were addressed in Scarlatti et al. (2023), while in this work we propose to extend its application allowing partially cloud conditions within the working sector of the image (which is now different and smaller). Therefore, we still rely on the principal plane signals to be processed by ML. This choice relies on the dependency between the radiance of the principal plane and the aerosol optical parameters (Olmo et al., 2008). Moreover, the principal plane presents a significant sensitivity to identify clouds within the region of interest in SONA images. In order to finally obtain the ML input, we have followed a three step, preprocessing flow: (A) crop-off the images (B) cloud identification and (C) generation of input signals.

(A) crop-off the images

As first step we crop-off the images and only viewing zenith angles less than 75° are used. This avoids the presence of buildings surrounding the station within the image. Then the images are rotated so that the principal plane is a vertical line with the Sun at the south. We define a small working sector for each image, that will be the only part of the image considered for the application of our retrieval methodology. It is defined by a 50-pixel width stripe, that has been symmetrically selected around the principal plane. Then we have considered different isolines of the scattering angle, varying from 14° to 82° in 2° steps, within the selected stripe (Fig. 1(a)). The 50-pixel width has been chosen as it represents the maximum width in which all the images of our dataset show left-to-right symmetry of the radiance with respect to the principal plane. Furthermore, the scattering angle range has been chosen to avoid the saturated pixels in the circumsolar region, in presence of large aerosol load, and to prevent exceeding the cropped part of the image at the lowest zenith angle reached in BASS. From now on we will only consider the defined sector of the image to deal with the cloud identification and to obtain the ML inputs. The main advantage in working only in this stripe of the image is that it does not matter what is the cloud coverage outside this relatively small region.

(B) cloud identification

We have developed a methodology to build a useful input signal for our ML model, even when clouds fall within our region of interest in the image (Fig. 1(a)). This methodology constitutes the novelty of this work and its most original part with respect to the state of art, and it is explained next. Given an all-sky camera image, an approximation of the plane signal is derived by averaging the radiance in each isoline of scattering angle within the considered sector of the image. This principal plane proxy signal is composed by 35 radiance values related to a well-defined scattering angle. This signal can be directly related to aerosol properties only in case that the whole sector is free of clouds (Scarlatti et al., 2023). Even if this averaged signal is smoothed, compared to the original principal plane signals, it may still account for some features that are not directly related to aerosol properties. For example, the presence of glitters in the principal plane associated to the optics of our camera (Laj et al., 2020), as well as some cloud contamination within the scene defined by the working sector of the image (Fig. 1(b)). Keeping in mind that we want to solve the problem of clouds within our working scene in the image, we identify those scattering angles which are partially or totally cloudy from our previously averaged signal, and flag them (Fig. 1(b)). This is the core of the cloud screening method, and we rely on two criteria based on: radiance symmetry and Blue-to-Red Ratio (BRR). Therefore, each isoline of scattering angle inside our working sector has been evaluated in terms of its radiative symmetry and BRR to ensure no presence of clouds inside them. To achieve it, we have defined two parameters, $\gamma_{sym}(i)$ and $\gamma_{brr}(i)$, related to the symmetry and BRR, respectively (1 and 2). L_i^+ and L_i^- represents the radiances symmetric with respect to principal plane at different all-sky camera channels (i=R,G,B), j is referred to single isoline and k to each pixel inside it:

$$\gamma_{sym}(i,j) = \frac{\sum_{k=1}^{\frac{1}{2}N} |L_i^+ - L_i^-|}{\overline{L_i(j)}} \tag{1}$$

$$\gamma_{brr}(j) = \frac{\sum_{k=1}^{N_j} \frac{L_B(k)}{L_R(k)}}{N_j} \tag{2}$$

Cloudy isolines of scattering angle inside the stripe sector show $\gamma_{sym}(j) > 0.04$ and γ_{brr} smaller than a specified threshold, which depends on the solar zenith angle and the scattering angle. The static threshold of 0.04 for γ_{sym} was obtained from the analysis of the γ_{sym} histogram for all the dataset of images, separating the symmetric peak from the skewed part of the distribution (Scarlatti et al., 2023). The width of the peak is indeed 0.04. Since both, cloudless and overcast scenarios, show very good symmetry within our working sector of the image, we need the γ_{brr} condition to separate them. The method to derive the dynamic γ_{brr} threshold has been the following: first, we obtain the averaged BRR for each isoline of scattering angle in cloud-free conditions for different solar zenith angles (SZA). We have used the SZA range in 2° steps. So, fixed a SZA we obtained from (2) the γ_{brr} with the varying scattering angles. Finally, we substract from each γ_{brr} the half of the standard deviation of γ_{brr} in each isoline. The last fundamental step is applied to avoid rejections of not cloudy but high aerosol load conditions. Indeed, for each isoline, a too high BRR threshold would include several cloudy isolines during the selection, something we should avoid. We would prefer instead to reject some clear isolines and consequently reconstruct his value in terms of averaged radiances, to obtain the desired signal. This criterion is a generalization of the method in Scarlatti et al. (2023) and represents just a trade-off between rejecting clouds and retaining high aerosol load areas of the sky.

(C) Generation of input signals

Once the cloudy points are identified, we take advantage of Pérez model (Perez et al., 1993) to reconstruct the RGB principal plane radiance at these cloudy points as if no clouds were present. The approach here is to use the radiance of the free-sky points of the signal

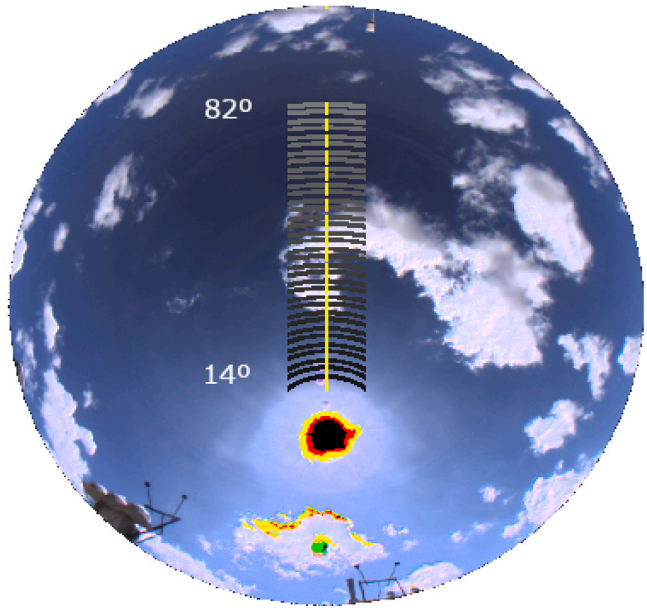

(a)

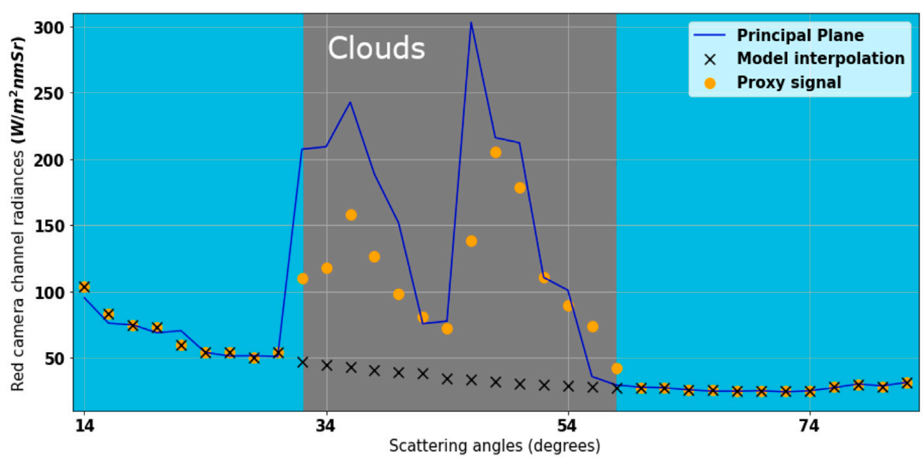

(b)

Fig. 1. (a) All-sky camera image of a partially cloud scenario on 02/09/2020, including our defined working sector of the image and the isolines of scattering angle (in gray). (b) Principal plane radiance for the all-sky camera image (blue line); single scattering isoline averaged values (orange dots) lastly, our ML input signal (black crosses) obtained from the fit of the Pérez model formula on free-sky points (orange dots on the blue part of the graph).

to fit the principal plane Pérez formula (3) and to obtain the radiance in the cloudy parts as if no clouds were there. (3) represents the particularization of the Pérez model to the principal plane developed by Chauvin et al. (2015), that is only dependent on the scattering angle (Θ) and the zenith angle of observation (θ).

$$L_{PP}(\Theta,\theta) = k(1 + a_1 e^{\frac{a_2}{\cos\theta}})(1 + b_1\Theta^{b_2} + b_3 \cos^2(\Theta + b_4)) \tag{3}$$

At least 7 points are needed to perform the fit since Eq. (3) contains 7 free parameters (k, a_1, a_2, b_1, b_2, b_3 and b_4). Consequently, and to ensure we have enough information from the cloud-free points, we have performed the Pérez fit only if at least 15 of them are available. This allows to obtain a convergent principal plane radiance with physical meaning. Sometimes the fit does not converge to realistic shapes of radiance in the principal plane even with the abovementioned restrictions. In particular, it tends to reach very high values at the extremes of scattering angles range. So we set a physical constrain and the fit is discarded if the radiance of any point of the signal exceeds 500 W/(m^2 sr nm) or it is negative. The upper limit has been set empirically, by analyzing the radiance in the blue channel on clear-sky days. The blue channel has been chosen since it shows the highest radiance, with a maximum value of 450 W/(m^2 sr nm). Considering all these restrictions, the fit generally converges and presents an excellent agreement with our proxy of the principal plane radiance (Fig. 1(b)). Once the fit is done, we have used the Pérez synthetic signal for the entire range of scattering angles as input for the ML. The simulated signal has some advantages since it perfectly reproduces the non-cloudy points of the signal already averaged for the principal plane and presents a smoothed shape (without any discontinuity or peaks) in the cloudy area. In addition, it allows using a homogeneous signal in all cases, which is independent of the sky conditions.

3.2. ML processing

A Gaussian Process Regressor (GPR) has been used as ML technique like we did in the previous work (Scarlatti et al., 2023), where the basic theory of the regressor is reported. In addition, we tested four

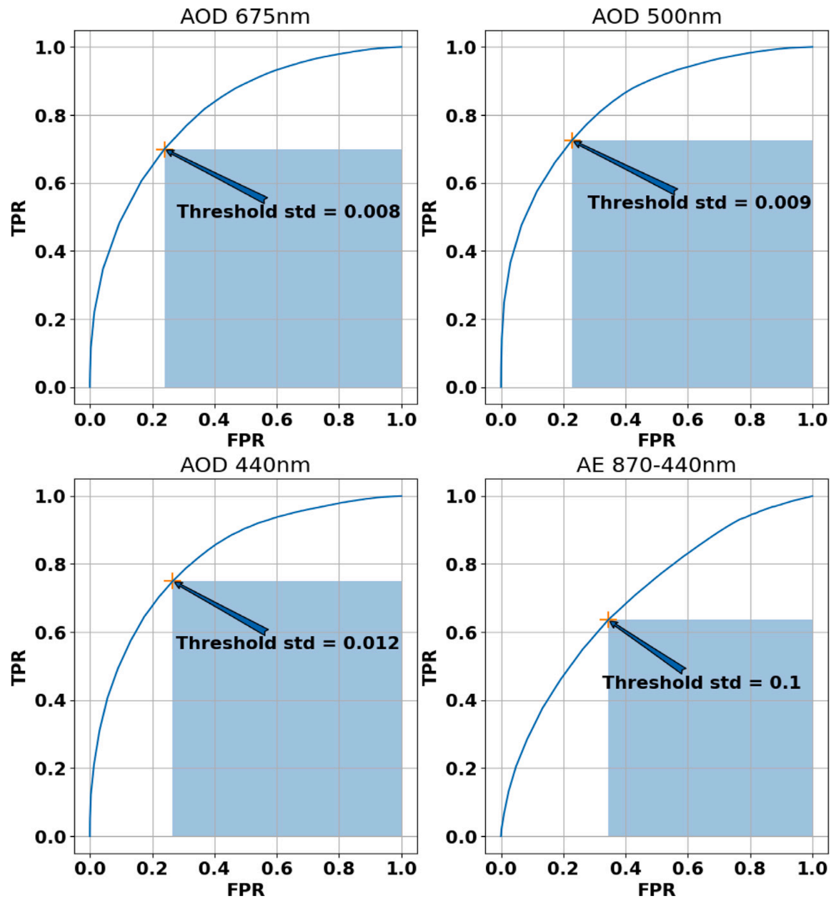

Fig. 2. TPR vs FPR curves for varying thresholds for different aerosol properties; (a) AOD at 675 nm; (b) AOD at 500 nm; (c) AOD at 400 nm and (d) AE. The threshold of standard deviation chosen for the data quality check is also highlighted for each figure, in correspondence with the point that maximize the area (1-FPR) * TPR (blue area).

different approaches to retrieve AOD and AE using a GPR, in Scarlatti et al. (2023). In the present study we only use one of them since it presented the best global performance in Scarlatti et al. (2023): RGB to AOD and BRR to AE. Therefore, the principal plane signal derived from each camera channel is used to predict the AOD at the closest AERONET wavelength. It means that the AOD at 675, 500 and 440 nm is predicted from the RGB signals, respectively. Moreover, the signal obtained from the BRR is used to predict the AE, derived from the combination of 675 and 440 nm AERONET filters. Considering the 2-year period database and the preprocessing conditions described in Section 3.1 we have 92,000 images that have been associated with the AERONET measurements. We have used 15,000 data (around 17% of the database) for the training of our four ML models. These training data have been randomly chosen to be representative of all the scenarios available in the whole period in terms of aerosol optical properties to be retrieved (AOD and AE). Finally, once the ML models have been trained, we apply them to perform AOD and AE predictions using the remaining 83% of the database. This step is called testing phase, and it is needed to assess the performance of our models over those remaining images.

3.3. Quality assurance

An additional and interesting feature of the GPR is its ability to propagate the statistical uncertainties based on the trained model. We use the standard deviation of these uncertainties to assess the quality of a single prediction. It is possible since the standard deviation of less accurate predictions is systematically larger than that corresponding to the accurate predictions (Scarlatti et al., 2023). Therefore, we can consider quality assured predictions if their standard deviation does not exceed a certain threshold. To determine the optimal threshold (th_0) for our predicted variables, AOD and AE, we use the Threshold-Moving method for imbalanced classification. It is an iterative method that is based on the analysis of a confusion matrix. To do this, the standard deviation threshold (th) is varied until an optimal value (th_0) is found, which maximizes the number of predictions that meet a certain number of conditions. In our case, the flow associated with this methodology is the following: given standard deviation threshold (th), we derive a confusion matrix, which is based on two conditions: (a) the standard deviation of the predictions is below (th); and (b) the predictions differ from the AERONET correspondent value by less than its nominal uncertainty (i.e., 0.01 and 0.1 for AOD and AE, respectively). The four elements of the confusion matrix are defined as: the True Positives (TP) are the number of predictions that simultaneously fulfill both conditions (a and b); the False Positives (FP) are the number of predictions that fulfill (a) but no (b); we consider True Negatives (TN) the number of predictions that do not meet either of the two conditions (a and b); finally the False Negatives (FN) are the predictions that does not meet with (a) but does (b). Then, we obtain the false positive rates (FPR) and true positive rates (TPR) for a given th, following (4) and (5).

$$FPR = \frac{FP}{FP + TN} \tag{4}$$

$$TPR = \frac{TP}{TP + FN} \tag{5}$$

This procedure is repeated varying th. For the AOD, th vary between 0.01 and 0.11, in steps of 0.001. Conversely, the range of th variation for AE is from 0.1 to 0.4 in 0.01 steps. The analysis of the variation of TPR in function of FPR for the varying thresholds (th) has been done independently for each of the predicted variables since they may have

Table 1
Statistics of the predicted aerosol properties in comparison with AERONET data. Results for the quality assured predictions are within the brackets. Nu_1 and Nu_2 are the percentage of predictions that differ from AERONET data less than 1x and 2x the nominal AERONET uncertainty, respectively.

	MAE	$RMSE$	$Nu_1(\%)$	$Nu_2(\%)$	$SLOPE \pm \delta$	$INTERCEPT \pm \delta$	R^2
AOD_{675}	0.009 (0.004)	0.019 (0.007)	75 (90)	90 (99)	0.983 (0.996) ± 0.001	0.0016 (0.0004) ± 0.0001	0.92 (0.98)
AOD_{500}	0.012 (0.005)	0.025 (0.008)	69 (88)	85 (97)	0.994 (0.996) ± 0.001	0.0016 (0.0007) ± 0.0001	0.91 (0.98)
AOD_{440}	0.015 (0.006)	0.029 (0.010)	63 (83)	80 (96)	1.018 (0.999) ± 0.001	−0.0009 (0.0003) ± 0.0002	0.90 (0.98)
AE	0.11 (0.05)	0.17 (0.10)	63 (77)	84 (98)	1.003 (1.002) ± 0.002	−0.007 (0.001) ± 0.002	0.80 (0.97)

a different behavior (Fig. 2). Finally, the optimal standard deviation threshold (th_0) has been chosen to maximize the area under the curve (1-FPR) x TPR (blue area in Fig. 2), since in this way the number of TP is maximum, and the FP is minimized. The th_0 chosen for each of the variables are labeled in Fig. 2. These values are very close to the AERONET uncertainties, even though they are derived in an independent way. In case of AOD a slight increase is observed for decreasing wavelength. Next the predictions with standard deviation smaller than the chosen th_0 are labeled as quality checked.

4. Results and discussion

4.1. Statistical evaluation of the model predictions

We have applied our ML models to the 2-year dataset of the all-sky camera imagery, from 10th February 2020 to 31st March 2022. We have used from 72,314 to 74,404 images, depending on the channel, that fulfill the criteria needed to apply our ML models in the test phase. On average, the 87% of the images correspond to clear-sky conditions and the remaining 13% present partial cloudiness within our work sector in the image. None of these images have been previously used to train the ML models. The ML model performance has been evaluated from the statistical results of the comparison with the correspondent AERONET data (Table 1 and Fig. 3). Our ML models show a good overall performance in predicting aerosol optical properties (Table 1) both, the whole dataset and the quality assured data. Considering the whole dataset, for AOD the RMSE and MAE are in general slightly higher than the AERONET uncertainties for all the predicted variables. In addition, more than 80% of our predictions from the whole set fall within the 2x AERONET nominal uncertainties, whereas it is substantially reduced if we consider 1x AERONET nominal uncertainties. For AOD, RMSE and MAE significantly decrease with increasing wavelength, while by the contrary the number of our predictions within the AERONET uncertainties (Nu_1 and Nu_2) and the correlation coefficients increase. This suggests a better performance of our models for longer wavelength channels. The application of the quality criteria substantially improves our ML results in the comparison against AERONET from all points of view (values between brackets in Table 1). On the one hand, the proportion of predictions within the AERONET uncertainties significantly increases, showing Nu_1 greater than 83% for AOD and 77% for AE. If we consider Nu_2 a notably improvement is observed up to 96% in all predicted variables. It is especially noticeable in the prediction of AE. On the other hand, the MAE and RMSE values are well below the AERONET measurement uncertainties, with an outstanding maximum MAE (RMSE) of 0.006 (0.010) for AOD at 440 and a 0.05 (0.01) for AE. The spectral differences observed in the statistics for the AOD predictions are reduced radically when the quality assured data are used. It is clearly observed in MAE and RMSE, as well as in the correlation coefficients, which all exceed 0.97, and in the slopes of the comparison, which are closer to unity for all the analyzed variables (Table 1).

When we do not impose quality assured criteria, our general results show good agreement with AERONET, although greater variability is observed (blue dots in Fig. 3). On the contrary, the comparison is excellent when we only use quality assured data (colored data superimposed in Fig. 3, where color indicates the density of points). Most of our quality assured data falls within the uncertainty of AERONET measurements (black lines in Fig. 3), and moreover the data spread is dramatically reduced for all the variables analyzed. However, the strict quality control that we apply to our ML observations results in a significant reduction in the number of available observations. Thus, the proportion of data that meet our quality criteria represents 53%–60% of the initial data, depending on the channel (Table 1). For example, for the red channel, it means that from the 72,608 initial dataset for the test step we have 43,740 quality assured available data. Of all of them, 42,635 correspond to clear skies and 1105 to partially cloudy conditions (just considering our work sector within the image). This implies that our strict quality criteria impact cloudy conditions images to a greater extent than those in clear skies. In fact, the number of cloudy images available is reduced by up to 94% of those we initially had. However, the maximum reduction in the number of clear sky images is 47% of the initial ones (Table 2). This reduction is different for each channel and the maximum values are observed for AE. These results are expected since our quality control method is mainly based on the variability of the results which is related to the standard deviation of the GPR. Generally, cloudy sky conditions present greater variability than clear sky conditions, even if we use a small portion of the image to carry out our analysis. With all this, clear sky images represent more than 97% of the quality-controlled images while cloudy images are less 2%, with slight differences among the channels (Table 2).

Finally, when AOD is available from the predictions, the Angstrom formula can be used to evaluate AE. In this case, the last training would not be needed. Even if not reported here, the authors performed this calculation and obtained large differences with respect to reference values, so this way is not practically usable. The Angstrom logarithmic formula largely propagates the existing differences between actual and predicted AOD, whereas, a complete new training on actual AE would not be affected by this issue. The computational time and resources are so negligible that the good results are worth the effort of performing further training to construct an AE model.

4.2. Sensitivity of ML model predictions to QA criteria

This work is mainly focused to predict AOD and AE, especially when clouds appear in our sector of interest in the image. The idea behind this objective is to increase the number of predictions, especially in cloudy sky conditions, with respect to the clear sky retrieval we previously published (Scarlatti et al., 2023). However, with the application of our strict quality criteria we only managed to save 6%–12% of these cloudy images, which at most are around 1000 (Table 2). Depending on the application for which our retrieval of aerosol properties is intended, it could be interesting to relax the conditions of our quality assurance method (e.g., simply because the problem of the study does not require so high accuracy, or because it is beneficial to increase the number of observations even at the cost of decreasing their quality). For this reason, we study what these new conditions imply, in relation to the number of data available and its quality. The most severe restriction of our quality assurance method is because we impose that the differences in our predictions must fall within the nominal uncertainty of the AERONET measurements (condition b, in Section 3.3. Therefore, to test the effect of our quality assurance method we rely only this condition b, by increasing the

Table 2
Number of data used for the complete dataset and quality-assured (QA) data for the test, separated for clear and cloudy conditions observed within our sector of interest of the image. The proportion of QA data with respect to the complete data test set is also reported (f), for total, clear and cloudy conditions. Moreover, the fraction clear and cloudy data from the total QA data is shown (η).

	Whole test dataset			Quality assured data						QA data	
	N_{cloudy}	N_{clear}	N_{total}	N_{cloudy}	N_{clear}	N_{total}	$f_{cloudy}(\%)$	$f_{clear}(\%)$	$f_{total}(\%)$	$\eta_{cloudy}(\%)$	$\eta_{clear}(\%)$
AOD_{675}	9184	63 424	72 608	1105	42 635	43 740	12	67	60	3	97
AOD_{500}	10 543	63 861	74 404	984	40 763	41 747	9	64	56	2	98
AOD_{440}	9024	63 463	72 487	914	41 383	42 297	10	65	58	2	98
AE	8932	63 382	72 314	507	37 741	38 248	6	60	53	1	99

Table 3
Sensitivity analysis of QA test set for the different channels. The optimum thresholds (th_0) on the predicted uncertainties and the number of QA images for cloudy (N_{cloudy}) and clear (N_{clear}) cases are reported. Nu_1 and Nu_2 represent the number of predictions within the 1x and 2 x AERONET uncertainties (0.01 for AOD and 0.1 for AE), and the rest of parameters have the same meaning that in Table 1. The last row for each channel refers to the values obtained when no quality criteria are used for the predictions, as the upper limit of the sensitivity analysis.

	b	th_0	MAE	$RMSE$	$Nu_1(\%)$	$Nu_2(\%)$	R^2	N_{cloudy}	N_{clear}
AOD_{675}	0.01	0.009	0.004	0.007	90	99	0.98	1105	42 635
	0.02	0.011	0.005	0.008	88	97	0.97	1682	50 106
	0.03	0.013	0.005	0.009	86	97	0.97	2239	54 333
	0.04	0.015	0.006	0.009	84	96	0.97	2728	56 900
	0.05	0.015	0.006	0.009	84	96	0.97	2728	56 900
	–	–	0.009	0.019	75	90	0.92	9184	63 424
AOD_{500}	0.01	0.010	0.005	0.008	88	97	0.98	984	40 763
	0.02	0.014	0.006	0.009	83	96	0.98	1733	51 430
	0.03	0.015	0.006	0.010	82	95	0.98	1913	52 929
	0.04	0.019	0.007	0.011	80	94	0.97	2610	56 882
	0.05	0.020	0.007	0.011	79	94	0.97	2771	57 499
	–	–	0.012	0.025	69	85	0.91	10 543	63 861
AOD_{440}	0.01	0.013	0.006	0.010	83	96	0.98	914	41 383
	0.02	0.016	0.007	0.011	79	94	0.98	1146	47 494
	0.03	0.019	0.007	0.012	76	93	0.97	1378	51 416
	0.04	0.020	0.007	0.012	76	92	0.97	1457	52 320
	0.05	0.022	0.008	0.012	75	91	0.97	1604	53 856
	–	–	0.015	0.029	63	80	0.90	9024	63 463
AE	0.1	0.13	0.05	0.010	77	98	0.97	507	37 741
	0.2	0.14	0.07	0.10	77	94	0.92	667	43 329
	0.3	0.15	0.07	0.11	75	93	0.91	835	47 448
	0.4	0.17	0.08	0.12	72	91	0.89	1198	53 275
	0.5	0.18	0.08	0.12	71	91	0.89	1385	55 088
	–	–	0.11	0.17	63	84	0.80	8932	63 382

difference we allow in our predictions with respect to the AERONET measurements. Specifically, the difference for AOD is changed between 0.01 to 0.05, in 0.01 steps. In case of AE, the difference varies from 0.1 to 0.5, in 0.1 steps. The rest of the methodology remains unchanged as explained in Section 3.3). Therefore, we obtain one different optimum threshold (th_0) for each of these steps. This analysis allows to relate our comparison results against AERONET measurements to the differences we allow in criterion b, and in turn, to monitor the number of cases that fall within its nominal uncertainty (Nu_1; or double, Nu_2). On the other hand, we also differentiate between the behavior of clear and partially cloudy sky conditions (N_{cloudy} and N_{clear}, respectively). The results of this sensitivity analysis are shown in Table 3.

As expected, applying any quality assurance criteria (even those less restrictive) implies a substantial reduction in the number of predictions, with respect to the complete dataset (i.e., no QA criteria applied, last row of each channel in Table 3). This behavior is observed in all channels and in all sky conditions, although to different extents (Table 3). In all cases, being more permissive by relaxing criterion b leads to an increase in the number of quality assured cases compared to the most restrictive case (i.e., the QA criteria applied in Section 3.1), first row of each channel in Table 3. In cloud-free conditions this increase does not present significant variation among the channels, with a factor around 1.3–1.5, from the first to the last step considered for criterion b. On the contrary, cloudy cases present greater variability depending on the considered channel and show higher increasing factors around 1.8–3, for the overall variation in criterion b. This means that by relaxing criterion b the number of AOD predictions in cloudy conditions increase from about 1000 (using the most restrictive criterion, 0.01 difference with AERONET measurements) to about 2700 in the red and green channels, and about 1600 in blue (when the most permissive criterion is used at b, 0.05) (Table 3). In the case of AE, the number of predictions in cloudy conditions increases from 507 to 1385 by relaxing the difference with AERONET from 0.1 to 0.5. The increase in the number of predictions by relaxing criterion b induces an increase in th_0 and a slight degradation in the quality of the available data in comparison to AERONET. Despite this, MAE, RMSE and R^2 indicate an excellent agreement between our predictions and AERONET observations for all channels. In particular, the MAE values are always below the AERONET nominal uncertainty, as a clear indicator of the good overall performance of our ML models. Even in the worst case, the correlation coefficients (R^2) are well above those obtained when quality control is not applied, with values higher than 0.97 and 0.89 for AOD and AE, respectively. It should be noted that more than 90% of our predictions show differences with AERONET smaller than 0.02 and 0.2, for AOD and AE, respectively. This happens regardless of the channel considered and even though criterion (b) is greatly relaxed, using in the worst case a distance with AERONET observations of up to 0.05 and 0.5, for AOD and AE, respectively. All these considerations demonstrate the stability of the ML models built in this work when predicting the properties of aerosols, and in turn the effectiveness of the quality criteria imposed as well as the methodology used. In addition, our sensitivity analysis allows choosing the optimal threshold of the standard deviation associated with the GPR (th_0) based

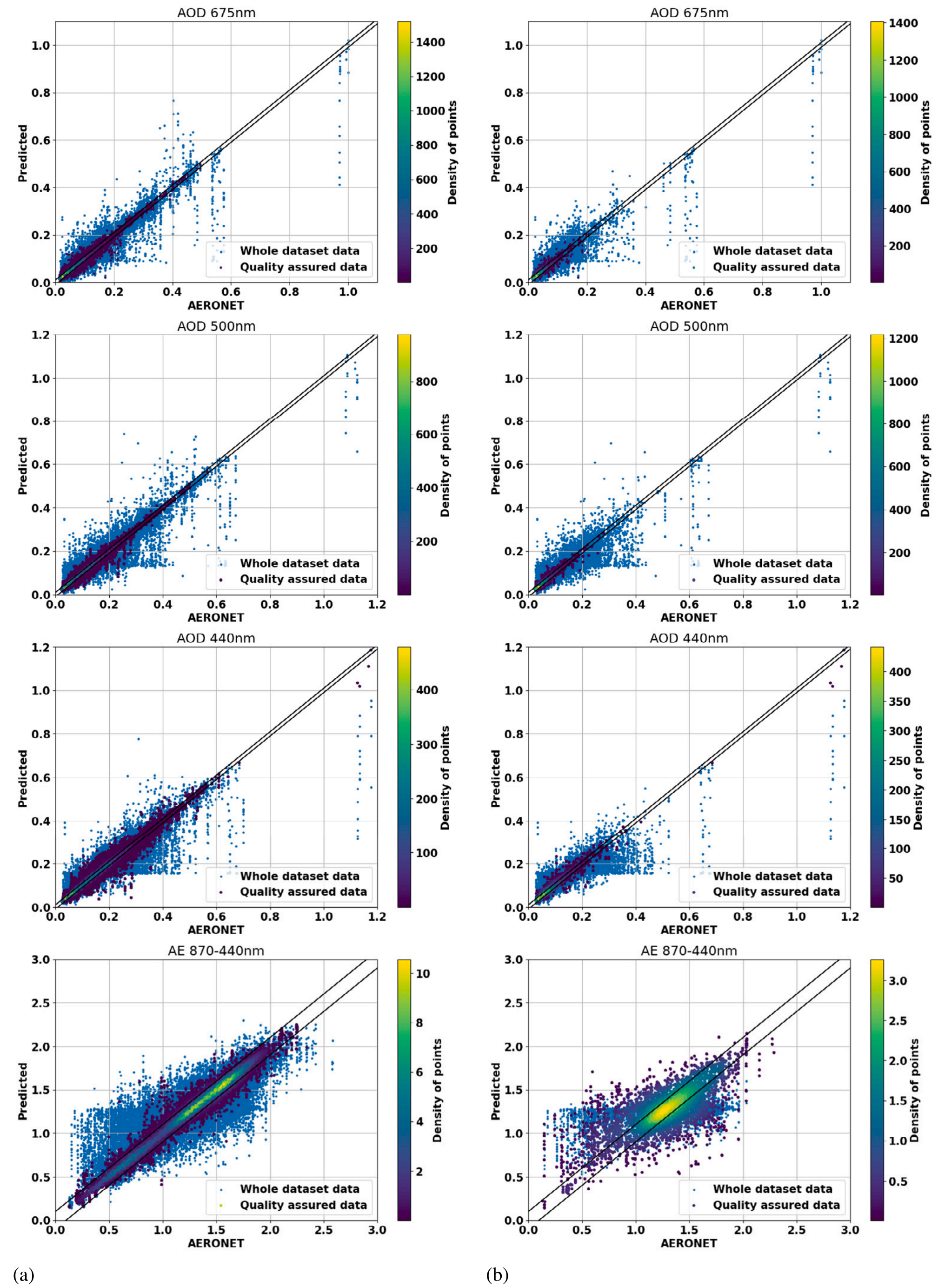

Fig. 3. (a) Scatterplot of ML predictions vs AERONET aerosol properties. The black lines represent the nominal AERONET uncertainty limits in AOD and AE. (b) The same graphs of (a) are reported only for cases in which partially cloudy scenes are used.

on the distance allowed with the AERONET measurements, depending on the desired application and the required level of accuracy. With all this we guarantee a good overall performance of our model predictions and the percentage of them within the AERONET uncertainties.

4.3. Sensitivity analysis of ML model predictions

The main objective of this work is to generalize the applicability of the methodology that we recently proposed in Scarlatti et al. (2023) to obtain the spectral AOD and AE using images from an all-sky imager. With this idea we intend that the method is useful in both, clear and partially cloudy skies. To achieve this, we have introduced some subtle methodological improvements with respect to Scarlatti et al. (2023), such as the shape and size of the image working sector, as well as a new cloud screening, which now is more rigorous. However, the most important differences lie in using synthetic signals from the Pérez model. It allows considering partially cloud conditions by avoiding cloudy spots within our working sector of the image. In contrast, only clear sky conditions are analyzed in Scarlatti et al. (2023). Finally, the method used to obtain the QA data has also been significantly improved compared to Scarlatti et al. (2023). With all these changes we obtain results that present high degree of agreement to the results reported in Scarlatti et al. (2023). This is especially evident when a QA method is applied since negligible differences are observed in MAE

Table 4
Statistics of the predicted aerosol properties in comparison with AERONET data only in partially cloud conditions. Results for the quality assured predictions are within the brackets. Nu_1 and Nu_2 are the percentage of predictions that differ from AERONET data less than 1x and 2x the nominal AERONET uncertainty, respectively.

	MAE	$RMSE$	$Nu_1(\%)$	$Nu_2(\%)$	$SLOPE \pm \delta$	$INTERCEPT \pm \delta$	R^2
AOD_{675}	0.023 (0.007)	0.046 (0.012)	42 (79)	64 (93)	1.070 (0.949) ± 0.007	−0.0060 (−0.0009) ± 0.0008	0.70 (0.85)
AOD_{500}	0.033 (0.005)	0.054 (0.008)	32 (83)	51 (95)	1.045 (0.943) ± 0.001	−0.0050 (0.0020) ±0.0005	0.71 (0.93)
AOD_{440}	0.037 (0.007)	0.059 (0.011)	28 (76)	46 (94)	1.116 (0.933) ± 0.001	−0.0107 (0.0031) ± 0.0007	0.72 (0.92)
AE	0.22 (0.08)	0.29 (0.13)	33 (76)	56 (92)	0.973 (0.991) ± 0.020	−0.027 (0.0027) ± 0.019	0.33 (0.91)

and R^2. In Scarlatti et al. (2023) we reported MAE values of 0.004, 0.005, 0.004 and 0.05, respectively for RGB and AE; whereas now we obtain 0.004, 0.005, 0.006 and 0.05 (Table 2). In both cases, (Scarlatti et al., 2023) and here, the QA data show R^2 over the 0.96, and the percentage of predictions within the AERONET uncertainty are higher than 73% of the used data. We have also performed some sensitivity analysis to analyze the effects associated to the methodological changes made in the current models, compared to those used in Scarlatti et al. (2023). In Scarlatti et al. (2023) we only work with clear sky images within our work sector. Therefore, first we have trained and tested again our models using only clear sky conditions. The results (not shown) indicate that the performance of the models is excellent, even slightly better to what was obtained in Scarlatti et al. (2023). This happens regardless to AOD and AE predictions and whether QA tests are applied or not. These differences are exclusively due to differences in the size and shape of the selected sector of the image, and to the cloud screening and quality control methods. Then, we conclude that all these improvements perform successfully, allowing us to improve performance of our previous results in Scarlatti et al. (2023). It must be considered that in our initial test dataset, the number of cases of clear sky represents 87% while that of cloudy sky is much lower, 13%. This suggests that the statistical characteristics of the comparison with AERONET shown in Tables 1 and 3 are mainly defined by the performance of the clear sky predictions. When we apply any quality control, even the least restrictive, the comparison with AERONET does not present a significant drift and still shows very good agreement (Table 3). This happens even though the percentage of cloudy sky cases varies substantially with the QA level. However, the percentage of cases of clear skies also varies and, although to a lesser extent, the absolute number of clear sky predictions is always much higher than that of cloudy scenes. All these variations may mask how cloudy conditions impact the comparison against AERONET. For this reason, we carry out some tests to regarding to the impact of using the Pérez model to synthetize signals in partially cloudy conditions. To do this, we have separately examined our results for clear and partly cloudy situations. As expected, in cloud-free conditions the statistics of the comparison with AERONET do not vary with respect to the general case (not shown). However, a decrease in the quality of the comparison results associated to cloudy predictions is observed Table 4 and Fig. 3b. Even so, the statistics show a significant improvement when the QA method is applied and a good agreement with AERONET is obtained. MAE is slightly higher than in the general case and remains below the AERONET nominal uncertainty, while RMSE is around them. Moreover, the percentage of predictions within the AERONET nominal uncertainties is higher than 76 and 92%, respectively for Nu_1 and Nu_2. The correlation coefficients are over 0.95, except for the AOD675. The radiative impact of clouds is usually greater for longer wavelengths, and this may explain the lower correlation observed in the red channel (Mejia et al., 2015).

Although our implementation of the Pérez model already includes a control procedure (Section 3.2), the statistical differences between the general and cloudy tests mostly rely on its reliability to fit our experimental data. It means that it may have a non-negligible impact on the prediction of AOD and AE under cloudy sky conditions, which is however minimized by applying the QAs. This analysis in partially cloudy scenes may have some implications to the overall behavior of our models since they have been trained without considering sky conditions. Thus, the training phase has been carried out mainly in clear sky conditions. The bias induced by this training may also contribute to the drift observed in the comparison statistics for cloudy predictions. A plausible solution to improve the performance of our ML models in partially cloudy cases would be to train them specifically in those conditions. Unfortunately, we do not have a sufficiently high amount of data in cloudy situations that meet the criteria imposed in the preprocessing to train the models with sufficient guarantees. Even so, we must keep in mind that the rest of the image (outside our work sector) can have any sky condition. Therefore, the high degree of agreement with AERONET supports that our methodology is a reliable alternative to address the optical properties of aerosols also in partial cloudy conditions. That is why the results obtained here are general and independent of the condition of the sky.

4.4. Comparison with other results

Other authors have derived the aerosols properties using all-sky camera images, both using physical methods (Román et al., 2022) and ML techniques (Cazorla et al., 2008, 2009; Logothetis et al., 2023). All of them consider only completely cloud-free images. In Román et al. (2022) a physical approach is used to retrieve spectral AOD and other aerosol size parameters combining all-sky camera images and a radiative transfer model. They rely on GRASP algorithm (Dubovik and King, 2000), which is used to perform the inversion of relative sky-radiance (uncalibrated), using the hybrid plane geometry. They report an accuracy of ± 0.02 for AOD smaller than 0.4 and good agreement in comparison with AERONET, using more than 2-year database (around 17,000 points). This comparison offers correlation coefficients (R^2) higher than 0.87. Regarding to the ML approaches, in Cazorla et al. (2008),Cazorla et al. (2009), a neural network is trained to derived spectral AOD and AE considering only a single significant radiance value at the scattering angle that better represent the principal plane signal. They use a very limited dataset around 1000 images and report a maximum of 80% of predictions fall within the AERONET uncertainties for AOD and AE. Another recent study (Logothetis et al., 2023) uses a supervised Gradient Boosting Machine algorithm to predict five aerosol parameters (spectral AOD, AE, Fine Mode Fraction) and aerosol type. The aerosol information is collected from the all-sky images using different points and geometries along with the percentage of saturated pixels around the Sun over the total number of pixels. Their predictions concur well with AERONET measurements, with correlation coefficients of 0.89–0.93 for spectral AOD and 0.92 for AE, as well as RMSE higher than 0.053. In general, our ML predictions show very good agreement with AERONET measurements and therefore are in line to those reported in the literature, both those using ML and Physics approaches (Cazorla et al., 2008, 2009; Román et al., 2022; Scarlatti et al., 2023; Logothetis et al., 2023). This happens for both, the spectral AOD and AE, even if we do not apply any QA criteria. However, our comparison substantially improves when we impose quality criteria and then the comparison with AERONET shows excellent results. It implies that our predictions clearly overperform all those reported in the literature when we apply any QA method, even in the least restrictive case. It should be highlighted that all the approaches described in Cazorla et al. (2008),Cazorla et al. (2009), Román et al. (2022),Logothetis et al. (2023) have been applied only under clear sky conditions. Therefore, the most important advantage of our new approach, is that we perform satisfactory predictions of aerosol optical properties in clear and partially cloud conditions (with specific criteria of selection that we discussed in the present paper). We have also implemented a quality control method that allows us to successfully control the quality of our results, according to the desired accuracy. On the other hand, the representativeness of our results is very general since we use a considerable amount of data, which notably exceed that used in other works (Cazorla et al., 2008, 2009; Román et al., 2022; Logothetis et al., 2023).

Finally, it is important to highlight that our ML models have been trained with specific calibrated radiances from HDR images. No other inputs than the radiance signals have been used to train the models and predict the aerosol properties. We provided no explicit information related to SZA, atmospheric composition or surface albedo in order to associate the radiance with AERONET retrievals. It is fundamental to point out that environmental or instrumental variability due to the calibration process is considered and absorbed by the models during the training process. With this in mind, the only constant parameter at our site is the surface albedo in the urban context. In principle, we cannot say if changing the location of the camera will produce significant errors in the aerosol properties prediction, even if the other environmental variability is similar to BASS. We performed a simple sensitivity analysis to evaluate the impact of the surface albedo on the radiance needed in our ML models. The objective here is to evaluate relative differences in radiance with respect to our site when changing surface albedo and other environmental variables such as SZA and AOD. If this relative difference is lower or comparable with the uncertainties in the radiance of the camera, we can conclude the model has absorbed this variability and the retrieval goodness is safe. We simulated, with the aid of a radiative transfer model (libRadtran), our principal plane radiance in different albedo scenarios. From the literature, we found that in urban and natural environments that do not account for extreme cases such as white deserts or ice and snow, the typical albedo values of the surface in the visible range (400–700 nm) do not exceed 0.15. In our simulations, at all the scattering angles of our signals (14°–82°), the relative differences with respect to our location radiance do not exceed 10%. This is actually the typical uncertainty related to the radiance in the red, green and blue channels of our calibrated camera. The uncertainty in radiance is therefore absorbed and considered by the model in the training phase, so we can conclude that these changes will have small effects on our retrieval.

5. Conclusions

A new methodology for retrieving aerosol optical properties from well calibrated all-sky camera images has been presented. This new approach combines a Gaussian Process Regression ML model trained using several random datasets chosen from colocated AERONET observations. It is based on that we recently proposed to predict AOD and AE when a small sector of the image, which contains the principal plane of the Sun, is cloud-free. However, our new approach is designed to be used also when clouds appear within our working sector in the image, and this is the main innovation of the present work. We have introduced additional novelties to address it. First the cloudy points are identified in our working sector and, an averaged and smoothed principal plane signal for the RGB radiances is derived by carefully analyzing its symmetry and shape. Then, a reliable methodology based on the Pérez model has been used to synthesize the principal plane signal in the cloudy spots. Finally, we use 2-year dataset to test the methodology in different atmospheric conditions regarding to the presence of clouds and aerosols, according to their amount and type. In addition, we have developed a method to assess the quality of predictions based on the standard deviation of the ML GPR method. This quality assurance method may be fine-tuned according to the desired accuracy based on the application for which it is intended. In general, we obtain AOD and AE predictions that present strong agreement with simultaneous AERONET measurements. Our predictions substantially improve when we apply our quality assurance method. In that case, more than 83% and 77% of the predictions fall within the nominal uncertainty associated with AERONET measurements for AOD and AE, respectively. This percentage significantly increases up to 96% in all predicted variables, when the double of AERONET uncertainties is considered. Furthermore, the comparison with AERONET shows a high degree of correlation, with R^2 greater than 0.97 and an overall MAE smaller than 0.006 and 0.05 for AOD and AE, which is well below the nominal uncertainty of AERONET observations. We have carried out a sensitivity analysis of every steps and processes implemented in our method that allow evaluating each of them separately, and in turn obtaining an overall assessment of their performance. This analysis indicates that:

1. Changes in size and shape of the working sector of the image have no significant impact in our predictions since the statistics results from the comparison against AERONET measurements for clear-sky cases improve our previously published results.

2. The comparison with AERONET deteriorates only slightly when the restrictions imposed for our quality assured data is more flexible and instead, we considerably increase the number of available images, especially in partly cloudy cases. Despite this, the comparison still offers excellent results even when the quality criterion is the least restrictive.

3. Cloudy scenes deteriorate the comparison with AERONET mainly due to the use of Pérez fit. However, this comparison improves substantially when the quality criteria is applied and the percentage of predictions within AERONET uncertainty is very high, up to 92%, for Nu_2.

These results confirm that our method is stable and not very sensitive to external and methodological factors, especially when we apply quality assurance criteria. All these considerations demonstrate the stability of the ML models built in this work to predict the properties of aerosols, and in turn the effectiveness of the quality criteria imposed as well as the methodology used. In addition, our new approach presents different advantages with respect to the state of the art reported in the literature. These are reflected in several aspects: both in their general applicability with independence on the sky conditions; in the quality, accuracy and stability of our predictions, as well as in increasing the number of available images. The camera has some advantages with respect to the sun photometer, such as the higher frequency of retrievals and the easier possibility of being moved to other locations with little or no significant difference in the goodness of the retrieval itself. With all this we guarantee a good overall performance of our model predictions that present a significant contribution to improve the versatility and operationality of all-sky cameras for aerosol remote sensing and their further use in atmospheric sciences, especially regarding to the study of aerosol-cloud interactions.

CRediT authorship contribution statement

F. Scarlatti: Writing – review & editing, Writing – original draft, Visualization, Validation, Software, Methodology, Investigation, Formal analysis, Conceptualization. **J.L. Gómez-Amo:** Writing – review & editing, Supervision, Resources, Project administration, Methodology, Funding acquisition, Conceptualization. **P.C. Valdelomar:** Resources, Data curation. **V. Estellés:** Writing – review & editing, Resources, Data curation. **M.P. Utrillas:** Writing – review & editing, Supervision, Project administration, Funding acquisition.

Declaration of competing interest

The authors declare that they have no known competing financial interests or personal relationships that could have appeared to influence the work reported in this paper.

Data availability

Data will be made available on request.

Acknowledgments

This work was funded jointly by the Spanish Ministry of Economy and Competitiveness (MINECO), Spain through the projects: RTI2018-096548-B-I00, PID2021-123881OB-I00, PID2022-138730OB-I00 and TED2021-129185BI00; and the Valencia Autonomous Government project, Spain: AICO/2021/341. We also acknowledge the COST Action CA21119 HARMONIA, supported by COST (European Cooperation in Science and Technology). The participation of F. Scarlatti has been supported by a PhD grant PRE2019-089986 funded by the Spanish Ministry of Science, Innovation and University, Spain.

Appendix. Statistical formulas

$$MAE = \frac{\sum_{i=1}^{N} |pred_i - meas_i|}{N} \tag{6}$$

$$RMSE = \sqrt{\frac{\sum_{i=1}^{N} (pred_i - meas_i)^2}{N}} \tag{7}$$

$$R^2 = 1 - \frac{\sum_{i=1}^{N} (pred_i - meas_i)^2}{\sum_{i=1}^{N} (pred_i - \overline{pred})^2} \tag{8}$$

References

Alexander, L., et al., 2013. Climate change 2013: The physical science basis, in contribution of working group I (WGI) to the fifth assessment report (AR5) of the intergovernmental panel on climate change (IPCC). In: Climate Change 2013: The Physical Science Basis.

Bao, F., et al., 2023. The retrieval of aerosol optical properties based on a random forest machine learning approach: Exploration of geostationary satellite images. Remote Sens. Environ. 286, 113426. http://dx.doi.org/10.1016/j.rse.2022.113426.

Calbó, J., et al., 2017. The thin border between cloud and aerosol: Sensitivity of several ground based observation techniques. Atmos. Res. 196, 248–260. http://dx.doi.org/10.1016/j.atmosres.2017.06.010.

Cazorla, A., et al., 2008. Using a sky imager for aerosol characterization. Atmos. Environ. 42 (11), 2739–2745. http://dx.doi.org/10.1016/j.atmosenv.2007.06.016, URL https://www.sciencedirect.com/science/article/pii/S1352231007005808. Vienna Visibility Conference 2006.

Cazorla, A., et al., 2009. Technical note: Determination of aerosol optical properties by a calibrated sky imager. Atmos. Chem. Phys. 9 (17), 6417–6427. http://dx.doi.org/10.5194/acp-9-6417-2009.

Chauvin, R., et al., 2015. Modelling the clear-sky intensity distribution using a sky imager. Sol. Energy 119, 1–17. http://dx.doi.org/10.1016/j.solener.2015.06.026.

di Sarra, A., et al., 2011. Shortwave and longwave radiative effects of the intense Saharan dust event of 25-26 March 2010 at Lampedusa (Mediterranean Sea): SAHARAN DUST RADIATIVE EFFECTS. J. Geophys. Res.: Atmos. 116 (D23), http://dx.doi.org/10.1029/2011jd016238.

di Sarra, A., et al., 2015. Empirical correction of multifilter rotating shadowband radiometer (MFRSR) aerosol optical depths for the aerosol forward scattering and development of a long-term integrated MFRSR-Cimel dataset at Lampedusa. Appl. Opt. 54 (10), 2725. http://dx.doi.org/10.1364/ao.54.002725.

Dubovik, O., King, M.D., 2000. A flexible inversion algorithm for retrieval of aerosol optical properties from Sun and sky radiance measurements. J. Geophys. Res.: Atmos. 105 (D16), 20673–20696. http://dx.doi.org/10.1029/2000jd900282.

Dubovik, et al., 2000. Accuracy assessments of aerosol optical properties retrieved from aerosol robotic network (AERONET) sun and sky radiance measurements. J. Geophys. Res.: Atmos. 105 (D8), 9791–9806. http://dx.doi.org/10.1029/2000jd900040.

Eck, T.F., et al., 2014. Observations of rapid aerosol optical depth enhancements in the vicinity of polluted cumulus clouds. Atmos. Chem. Phys. 14 (21), 11633–11656. http://dx.doi.org/10.5194/acp-14-11633-2014.

Eddy, C., 2012. Aerosol direct radiative forcing: A review. In: Atmospheric Aerosols - Regional Characteristics - Chemistry and Physics. InTech, http://dx.doi.org/10.5772/50248.

Estellés, V., et al., 2007. Columnar aerosol properties in Valencia (Spain) by ground-based Sun photometry. J. Geophys. Res.: Atmos. 112 (D11), http://dx.doi.org/10.1029/2006jd008167.

Fiorentin, P., et al., 2020. Calibration of digital compact cameras for sky quality measures. J. Quant. Spectrosc. Radiat. Transfer 255, 107235. http://dx.doi.org/10.1016/j.jqsrt.2020.107235, URL https://www.sciencedirect.com/science/article/pii/S0022407319309276.

Giles, D.M., et al., 2019. Advancements in the aerosol robotic network (AERONET) version 3 database – automated near-real-time quality control algorithm with improved cloud screening for Sun photometer aerosol optical depth (AOD) measurements. Atmos. Meas. Tech. 12 (1), 169–209. http://dx.doi.org/10.5194/amt-12-169-2019.

Gómez-Amo, J., et al., 2017. Impact of dust and smoke mixing on column-integrated aerosol properties from observations during a severe wildfire episode over Valencia (Spain). Sci. Total Environ. 599–600, 2121–2134. http://dx.doi.org/10.1016/j.scitotenv.2017.05.041.

Gómez-Amo, J., et al., 2019. Empirical estimates of the radiative impact of an unusually extreme dust and wildfire episode on the performance of a photovoltaic plant in Western Mediterranean. Appl. Energy 235, 1226–1234. http://dx.doi.org/10.1016/j.apenergy.2018.11.052.

González, J.A., et al., 2023. Assessment of cloudless-to-cloud transition zone from downwelling longwave irradiance measurements. Atmos. Res. 285, 106657. http://dx.doi.org/10.1016/j.atmosres.2023.106657, URL https://www.sciencedirect.com/science/article/pii/S0169809523000546.

Guo, B., et al., 2023. Reconstructing MODIS aerosol optical depth and exploring dynamic and influential factors of AOD via random forest at the global scale. Atmos. Environ. 315, 120159. http://dx.doi.org/10.1016/j.atmosenv.2023.120159, URL https://www.sciencedirect.com/science/article/pii/S135223102300585X.

Kim, D., Ramanathan, V., 2008. Solar radiation budget and radiative forcing due to aerosols and clouds. J. Geophys. Res.: Atmos. 113 (D2), http://dx.doi.org/10.1029/2007jd008434.

Laj, et al., 2020. A global analysis of climate-relevant aerosol properties retrieved from the network of global atmosphere watch (GAW) near-surface observatories. Atmos. Meas. Tech. 13 (8), 4353–4392. http://dx.doi.org/10.5194/amt-13-4353-2020.

Logothetis, S.A., et al., 2023. Aerosol optical properties and type retrieval via machine learning and an all-sky imager. Atmosphere 14 (8), 1266. http://dx.doi.org/10.3390/atmos14081266.

Luffarelli, M., et al., 2022. Aerosol optical thickness retrieval in presence of cloud: Application to S3A/SLSTR observations. Atmosphere 13 (5), 691. http://dx.doi.org/10.3390/atmos13050691.

Marcos, C.R., et al., 2018. Analysis of four years of ceilometer-derived aerosol backscatter profiles in a coastal site of the western Mediterranean. Atmos. Res. 213, 331–345. http://dx.doi.org/10.1016/j.atmosres.2018.06.016.

Mejia, F.A., et al., 2015. Coupling sky images with three-dimensional radiative transfer models: A new method to estimate cloud optical depth. http://dx.doi.org/10.5194/amtd-8-11285-2015.

Olmo, F.J., et al., 2008. Retrieval of the optical depth using an all-sky CCD camera. Appl. Opt. 47 (34), H182. http://dx.doi.org/10.1364/ao.47.00h182.

Perez, R., et al., 1993. All-weather model for sky luminance distribution—Preliminary configuration and validation. Sol. Energy 50 (3), 235–245. http://dx.doi.org/10.1016/0038-092x(93)90017-i.

Peris-Ferrús, C., et al., 2021a. Retrieval of cloud optical depth: Synergies between whole sky imagers and radiative transfer modeling. In: Comerón, A., Kassianov, E.I., Schäfer, K., Picard, R.H., Weber, K., Singh, U.N. (Eds.), Remote Sensing of Clouds and the Atmosphere XXVI. SPIE, http://dx.doi.org/10.1117/12.2599586.

Peris-Ferrús, C., et al., 2021b. Retrieval of cloud optical depth through radiative transfer and remote sensing: from 1D to 3D approach. In: Comerón, A., Kassianov, E.I., Schäfer, K., Picard, R.H., Weber, K., Singh, U.N. (Eds.), Remote Sensing of Clouds and the Atmosphere XXVI. SPIE, http://dx.doi.org/10.1117/12.2599591.

Román, R., et al., 2012. Calibration of an all-sky camera for obtaining sky radiance at three wavelengths. Atmos. Meas. Tech. 5 (8), 2013–2024. http://dx.doi.org/10.5194/amt-5-2013-2012.

Román, R., et al., 2022. Retrieval of aerosol properties using relative radiance measurements from an all-sky camera. Atmos. Meas. Tech. 15 (2), 407–433. http://dx.doi.org/10.5194/amt-15-407-2022.

Scarlatti, F., et al., 2021. Retrieving aerosol properties using signals from an all-sky camera and a random forest model. In: Comerón, A., Kassianov, E.I., Schäfer, K., Picard, R.H., Weber, K., Singh, U.N. (Eds.), Remote Sensing of Clouds and the Atmosphere XXVI. SPIE, http://dx.doi.org/10.1117/12.2599854.

Scarlatti, F., et al., 2023. A machine learning approach to derive aerosol properties from all-sky camera imagery. Remote Sens. 15 (6), 1676. http://dx.doi.org/10.3390/rs15061676.

Segura, S., et al., 2016. Multiyear in-situ measurements of atmospheric aerosol absorption properties at an urban coastal site in western Mediterranean. Atmos. Environ. 129, 18–26. http://dx.doi.org/10.1016/j.atmosenv.2016.01.008.

Sicard, M., et al., 2012. Intense dust and extremely fresh biomass burning outbreak in Barcelona, Spain: Characterization of their optical properties and estimation of their direct radiative forcing. Environ. Res. Lett. 7 (3), 034016. http://dx.doi.org/10.1088/1748-9326/7/3/034016.

Sicard, M., et al., 2014. Estimation of mineral dust long-wave radiative forcing: Sensitivity study to particle properties and application to real cases in the region of Barcelona. Atmos. Chem. Phys. 14 (17), 9213–9231. http://dx.doi.org/10.5194/acp-14-9213-2014.

Smirnov, A., et al., 2000. Cloud-screening and quality control algorithms for the AERONET database. Remote Sens. Environ. 73 (3), 337–349. http://dx.doi.org/10.1016/s0034-4257(00)00109-7.

Tian, X., et al., 2022. Retrieval of atmospheric aerosol optical depth from AVHRR over land with global coverage using machine learning method. IEEE Trans. Geosci. Remote Sens. 60, 1–12. http://dx.doi.org/10.1109/tgrs.2021.3129853.

Valdelomar, P., et al., 2021. Feasibility of ground-based sky-camera HDR imagery to determine solar irradiance and sky radiance over different geometries and sky conditions. Remote Sens. 13 (24), 5157. http://dx.doi.org/10.3390/rs13245157.

Yang, C.K., et al., 2022. Near-cloud aerosol retrieval using machine learning techniques, and implied direct radiative effects. Geophys. Res. Lett. 49 (20), http://dx.doi.org/10.1029/2022gl098274.